JCB Journal of Cell Biology

ARTICLE

Myosin IIB assembly state determines its mechanosensitive dynamics

Eric S. Schiffhauer[1], Yixin Ren[1], Vicente A. Iglesias[5], Priyanka Kothari[1], Pablo A. Iglesias[1,5], and Douglas N. Robinson[1,2,3,4]

Dynamical cell shape changes require a highly sensitive cellular system that can respond to chemical and mechanical inputs. Myosin IIs are key players in the cell's ability to react to mechanical inputs, demonstrating an ability to accumulate in response to applied stress. Here, we show that inputs that influence the ability of myosin II to assemble into filaments impact the ability of myosin to respond to stress in a predictable manner. Using mathematical modeling for *Dictyostelium* myosin II, we predict that myosin II mechanoresponsiveness will be biphasic with an optimum established by the percentage of myosin II assembled into bipolar filaments. In HeLa and NIH 3T3 cells, heavy chain phosphorylation of NMIIB by PKCζ, as well as expression of NMIIA, can control the ability of NMIIB to mechanorespond by influencing its assembly state. These data demonstrate that multiple inputs to the myosin II assembly state integrate at the level of myosin II to govern the cellular response to mechanical inputs.

Introduction

In many essential cellular shape change processes, including cell migration, cytokinesis, and tissue development, chemical and mechanical signals integrate to allow morphogenic fidelity. For example, the mechanical activation of integrins on stiff substrates activates the Cdc42–mPAR6–PKCζ pathway, which is critical for setting the position of the microtubule organizing center and organelles in polarized cell migration (Etienne-Manneville and Hall, 2001; Gomes et al., 2005). Inside the cell, nonmuscle myosin II (NMII) also senses and accumulates in response to mechanical inputs during cytokinesis and cell migration, which allows for the proper spatial localization and function of the protein (Finer et al., 1994; Uyeda et al., 2011; Kee et al., 2012; Luo et al., 2012, 2013; Raab et al., 2012; Schiffhauer et al., 2016). Interestingly, signaling pathways, such as Cdc42–mPAR6–PKCζ, can directly impact the dynamics of the NMII pool (Even-Faitelson and Ravid, 2006; Juanes-García et al., 2015). Understanding how this chemical regulation affects the ability of NMII to bind specifically to actin filaments experiencing mechanical load is key to determining the molecular mechanism by which NMII is tuned to localize correctly in cells during shape change processes.

NMII contains individual hexamers comprising two heavy chains containing motor and coiled-coil domains, two regulatory light chains (RLCs), and two essential light chains, henceforth referred to as "functional monomers" (De la Roche et al., 2002; Vicente-Manzanares et al., 2009). These functional monomers form into dimers, then tetramers, and ultimately assemble into functional bipolar filaments, consisting of up to 20–30 subunits with high avidity for actin filaments and ability to exert contractile force (De la Roche et al., 2002; Billington et al., 2013). NMII's ability to assemble and disassemble are critical for its localization to sites of stress in the cell and for ensuring proper cytokinesis furrow ingression and cell body translocation during migration (De la Roche et al., 2002; Vicente-Manzanares et al., 2009; Poirier et al., 2012). In addition, the ability of NMII to bind actin filaments in a force-dependent manner allows specific localization of the protein to filaments under load (Finer et al., 1994; Uyeda et al., 2011; Kee et al., 2012; Luo et al., 2012; Schiffhauer et al., 2016). However, the direct relationship between myosin II's filament turnover and the ability to accumulate in response to mechanical stress remains unclear.

In the social amoeba *Dictyostelium discoideum*, the regulation of myosin II turnover and localization during cytokinesis and motility is controlled by the phosphorylation of three threonine residues in the myosin II heavy chain helical tail region by the myosin heavy chain kinases (MHCKA, MHCKB, MHCKC, and MHC KD; Yumura et al., 2005). A mutant myosin II protein containing aspartic acids at all three threonine residues to mimic phosphorylation (3× Asp) forms very limited bipolar filaments in vitro, shows very little enrichment in the actin cortex in cells, and does

[1]Department of Cell Biology, School of Medicine, Johns Hopkins University, Baltimore, MD; [2]Department of Pharmacology and Molecular Sciences School of Medicine, Johns Hopkins University, Baltimore, MD; [3]Department of Medicine, School of Medicine, Johns Hopkins University, Baltimore, MD; [4]Department of Chemical and Biomolecular Engineering, Whiting School of Engineering, Johns Hopkins University, Baltimore, MD; [5]Department of Electrical and Computer Engineering, Whiting School of Engineering, Johns Hopkins University, Baltimore, MD.

Correspondence to Douglas N. Robinson: dnr@jhmi.edu.

https://doi.org/10.1083/jcb.201806058

not accumulate at the furrow during cytokinesis (Sabry et al., 1997; De la Roche et al., 2002; Ren et al., 2014). In contrast, a myosin II mutant protein containing nonphosphorylatable alanine residues at the three critical threonines (3× Ala) shows higher assembly into bipolar filaments than WT and over-accumulates in the cell cortex and cleavage furrow (Sabry et al., 1997; De la Roche et al., 2002; Ren et al., 2009). To emulate the mechanical stresses that cells produce internally or experience externally without probing substrate adhesion-based signaling, we used micropipette aspiration (MPA). MPA allows precise physiological mechanical stresses to be applied across a well-defined surface area, typically 20–30 μm^2, at a well-defined initial time point. This approach allows quantitative assessment of a cell's molecular responses to mechanical inputs. Using this method, WT GFP-MyoII accumulates in response to imposed stress, but the under-assembled GFP–3× Asp and the over-assembled GFP–3× Ala mutants do not (Ren et al., 2009). This result indicates a critical relationship between myosin II assembly/disassembly dynamics and mechanoresponsiveness and that the myosin II assembly state and mechanoresponse is controlled by myosin heavy chain kinase activity.

In mammalian cells, the three NMII paralogs (NMIIA, NMIIB, and NMIIC) are regulated by RLC and heavy chain phosphorylation (Vicente-Manzanares et al., 2009; Dulyaninova and Bresnick, 2013). Spatially broad, force-dependent activation of NMII through phosphorylation of the RLC has been demonstrated (Vicente-Manzanares et al., 2009; Schiller et al., 2013). Certainly, RLC phosphorylation is required for myosin II mechanoresponsiveness in *Dictyostelium*, *Drosophila melanogaster*, and mammalian cells (Ren et al., 2009; Kim et al., 2015; Schiffhauer et al., 2016). Inhibition of RLC phosphorylation by inhibiting calcium-activated MLCK or RhoA-activated ROCK inactivates and prevents force-dependent accumulation of all three mammalian NMIIs (Schiffhauer et al., 2016). However, RhoA, ROCK, and MLCK do not show mechanosensitive accumulation, and calcium signaling is not required for myosin's mechanoaccumulation (Luo et al., 2013; Kim et al., 2015; Schiffhauer et al., 2016). Thus, even though RLC phosphorylation is essential for activating myosin, it does not specifically direct myosin binding to actin filaments experiencing tension. Instead, mechanical stress directly promotes the cooperative binding of myosin II to actin in *Dictyostelium*, *Drosophila*, and mammalian cells (Orlova and Egelman, 1997; Kovács et al., 2007; Fernandez-Gonzalez et al., 2009; Tokuraku et al., 2009; Uyeda et al., 2011; Luo et al., 2012; Kim et al., 2015; Schiffhauer et al., 2016).

Furthermore, the mammalian NMIIs show paralog-specific regulation of mechanoresponsiveness. The peak accumulation of NMIIA and NMIIC during MPA is very similar across multiple mammalian cell types and across the cell cycle. However, the peak accumulation of NMIIB is differentially regulated across cell types and phases of the cell cycle (Schiffhauer et al., 2016). This myosin paralog-specific mechanoresponsiveness, in combination with the importance of heavy chain regulation–dependent mechanoresponse in *Dictyostelium* (Ren et al., 2009), led us to investigate the influence of NMIIB heavy chain phosphoregulation on mechanoresponsiveness.

The NMII heavy chain tail is phosphorylated by PKC, casein kinase II, and TRPM7 enzymes (Vicente-Manzanares et al., 2009). Phosphorylation of the NMIIA tail by PKCβ results in paralog-specific binding by S100A4 (or metastasin 1; Mts1) and increased NMIIA filament turnover (Dulyaninova et al., 2005). For NMIIB, paralog-specific phosphorylation by the atypical PKCζ leads to slower filament assembly and altered NMIIB organization in cells (Even-Faitelson and Ravid, 2006). Phosphomimetic NMIIB mutants mimicking PKCζ phosphorylation (1935D) show faster turnover in cells by FRAP and altered localization during migration (Juanes-García et al., 2015). NMIIB localization is PKCζ-dependent, as an overactive version of the kinase (myristoylated PKCζ) alters the morphology of migrating cells expressing WT NMIIB, but has no effect on cells expressing the nonphosphorylatable mutant, NMIIB 1935A (Juanes-García et al., 2015). Here, we show that the fraction of NMIIB assembled into bipolar filaments that associates with the actin cytoskeleton determines its mechanoresponsiveness. PKCζ-dependent heavy chain phosphorylation and other factors that influence NMIIB assembly state, such as coassembly with NMIIA, help define this assembly fraction of NMIIB, thereby specifying the ability of NMIIB to mechanorespond in a predictable manner.

Results

Myosin II heavy chain phosphorylation controls mechanoresponse in *Dictyostelium* in a biphasic manner

To begin to decipher how NMIIB could show different mechanoresponsiveness in different systems, we noticed a trend from published data in the *Dictyostelium* system that provides powerful insight. In Ren et al. (2009), myosin II heavy chain–null *(myoII*; specifically null for the *mhcA* gene) *Dictyostelium* cells expressing N-terminal GFP-labeled WT myosin II were aspirated by MPA, and the GFP-myoII responded by accumulating in the pipette in response to the applied stress (Fig. 1 A). In contrast, GFP–3× Asp or GFP–3× Ala proteins did not accumulate in response to applied stress (Fig. 1 A). Mechanoresponsiveness for these mutants in the MPA assay was quantified using a ratio of the peak background-corrected fluorescence intensity in the pipette to the intensity of the cortex at the opposite side of the cell (I_p/I_o), with both measurements collected at the same time (Ren et al., 2009). Cytoskeletal association of these mutants had also been measured previously via cytoskeletal fractionation (Rai and Egelhoff, 2011). When we compiled these observations by plotting the mechanoresponsiveness as a function of percentage of myosin II in the cytoskeletal fraction, we observed that very poor mechanoresponsiveness was observed when myosin II cytoskeletal association was low (12%; GFP–3× Asp) or high (47%; GFP–3× Ala; Fig. 1 B). However, WT GFP-myoII had high mechanoresponsiveness but intermediate cytoskeletal association (21%; WT GFP-myoII).

To further understand this relationship between degree of cytoskeletal association and the myosin II's mechanoresponsiveness, we leveraged a computational model we developed previously to describe mechanosensitive accumulation of myosin II in *Dictyostelium* (Luo et al., 2012, 2013; Mohan et al., 2015). The model describes bipolar filament formation from the monomers to filaments, consisting of up to 36 dimers in the mature bipolar filaments (*Dictyostelium* myosin II bipolar filaments are thought to contain up to 72 monomers; Mahajan and Pardee, 1996).

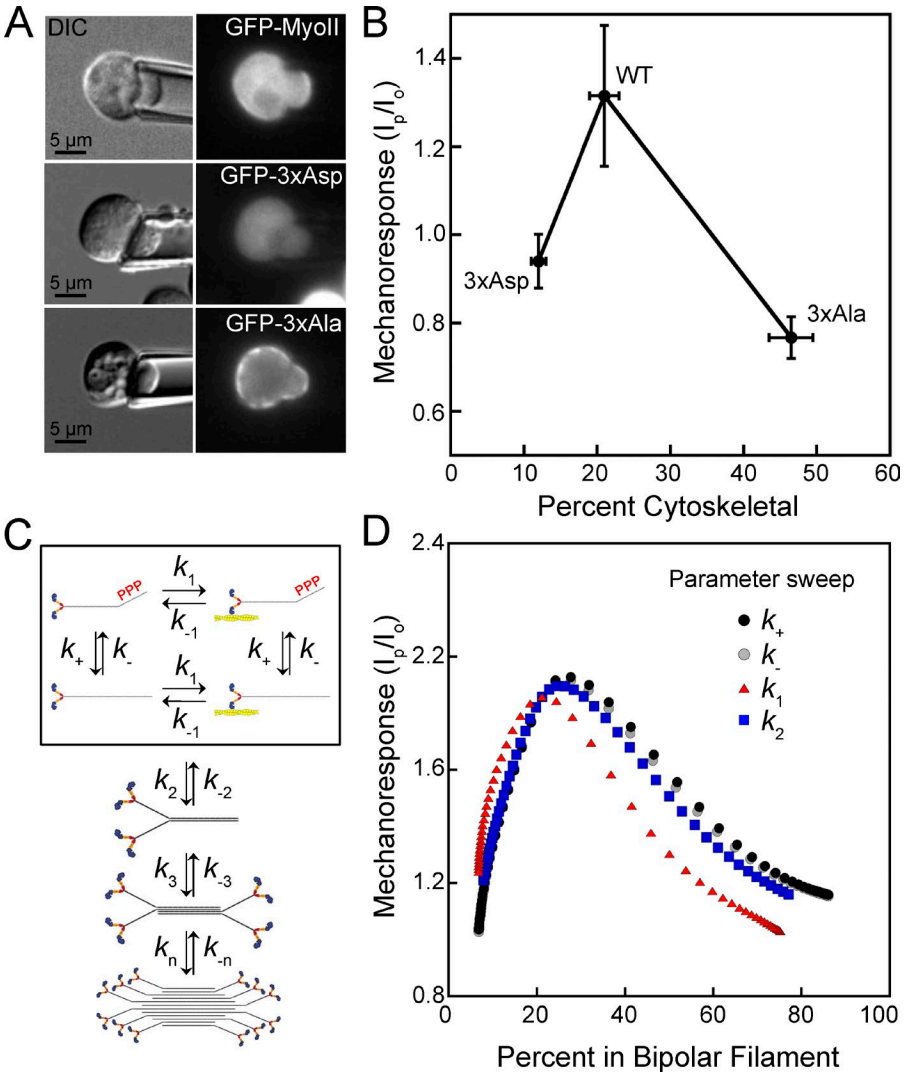

Figure 1. **Myosin II cytoskeletal association and mechanoresponsiveness have a biphasic relationship in *Dictyostelium*. (A)** GFP-MyoII accumulates to the region of the cell dilated by the pipette upon applied force. Mutant myosin II proteins mimicking heavy chain phosphorylation (GFP–3× Asp) or nonphosphorylatable mutants (GFP–3× Ala) do not respond to the applied force. **(B)** Mechanoresponsiveness suggests a biphasic dependency on the percentage of myosin that is cytoskeleton-associated. Peak myosin II mechanoresponse is calculated as the highest ratio of background-subtracted intensity in the pipette (I_p) to the background-subtracted intensity at the cortex at the opposite side of the cell (I_o) in 5 min. Mechanoresponse values (y axis values) reproduced from Ren et al. (2009). Percent cytoskeletal is measured by cytoskeletal fraction and reproduced from Rai and Egelhoff (2011) with permission from the authors (x axis values). **(C)** Scheme to model the assembly of myosin II bipolar filaments, including exchange between assembly-incompetent, assembly-competent, actin-bound, and actin-unbound monomers (boxed). Monomers then assemble into dimers, tetramers, and bipolar filaments. **(D)** A computational model for myosin II mechanosensitive assembly predicts that when increased or decreased by an order of magnitude, rates affecting myosin II transition from assembly-incompetent to assembly-competent (k_+ and k_-), from actin unbound to actin bound (k_1), or from monomer to dimer (k_2) will reproduce a biphasic relationship between the percent of myosin II assembled and the mechanoresponse at 5 min.

Monomers were assumed to be in one of four states, depending on whether they are bound to actin or not and/or assembly-competent or -incompetent, based on heavy chain phosphorylation (Fig. 1 C). We also considered that the detachment of bound myosin from actin is force sensitive (k_{-1}). Spatially, we compartmentalized the cell into three regions: the cytoplasm and two separate cortex regions, depending on whether the cortical regions were under mechanical stress or not. Simulations were first used to compute the fraction of myosin in filaments in the absence of mechanical stress. We started with previously published measured parameters from *Dictyostelium,* including the concentration of myosin II and the rate of monomer diffusion in cells. The baseline rates of conversion from assembly-incompetent monomers to assembly-competent monomers (k_+ and k_-) and from actin bound to actin unbound (k_1 and k_{-1}) result in filament assembly state that matches a WT *Dictyostelium* cell, where the fraction of myosin in bipolar filaments is 21% (where all curves meet in Fig. 1 D; x axis). At this assembly state, upon application of force to the region under stress, the model predicted the amount of myosin II in the stressed region to be 1.9-fold higher than the unstressed region (where all curves meet in Fig. 1 D; y axis). Changing the k_+ or k_- rate is analogous to changing the rate at which myosin II gets phosphorylated on its heavy chain, and when these two rates were made faster or slower in small increments, the model recapitulated the assembly states of the 3× Asp and 3× Ala mutants and every assembly state in between (Fig. 1 D; k_+ or k_- curves and x axis). Phosphorylation of the myosin II heavy chain was also expected to change the rate at which monomers assemble to form dimers, k_2. Making this rate faster or slower incrementally also resulted in assembly states from 5 to 80%. As k_+, k_-, or k_2, which are related to levels of phosphorylation of the myosin II heavy chain, were adjusted up and down, mechanoresponse showed an optimum near 20–25%, with poor mechanoresponse on both ends of the biphasic curve (Fig. 1 D). While not directly replicating the effect of heavy chain phosphorylation, changing the on rate of actin binding for myosin monomers, k_1, also resulted in assembly states between 5 and 80% (Fig. 1 D; x axis). While the shape of the curve for the k_1 parameter differs slightly from that of k_+, k_-, and k_2, changing this rate also predicted a biphasic relationship between assembly state and mechanoresponse (Fig. 1 D). This implies that a biphasic relationship between assembly state and mechanoresponse is fundamental, and any changes in rates that affect assembly state likely alter myosin II's mechanoresponsiveness in a predictable manner.

NMIIB cytoskeletal enrichment predicts mechanoresponsiveness in mammalian cells in a biphasic manner

To investigate the cell type–specific mechanoresponsiveness of NMIIB demonstrated previously (Schiffhauer et al., 2016) and in light of the impact of myosin II cytoskeletal association on mechanoresponsiveness observed in *Dictyostelium* (Fig. 1; Ren et al., 2009; Rai and Egelhoff, 2011), we quantified the cytoskeletal association of myosin II in HeLa, Jurkat, and NIH 3T3 cells. HeLa, Jurkat, and NIH 3T3 cells were resuspended and rotated for 10 min to replicate the conditions of MPA, then gently lysed and subjected to cytoskeletal fractionation. The cytoskeletal and supernatant fractions were probed for NMIIA or NMIIB (Fig. 2 A). All three cell types showed <10% association of NMIIA with the cytoskeleton and a stronger cytoskeletal association of NMIIB than NMIIA (Fig. 2 B). HeLa cells showed the highest NMIIB cytoskeletal association (27 ± 2.8%), followed by Jurkat cells (17 ± 1.3%) and NIH 3T3 cells (4.3 ± 0.81%; Fig. 2 B). Peak NMIIB mechanoresponse in 5 min demonstrated biphasic behavior as a function of cytoskeletal association, reminiscent of the relationship seen in *Dictyostelium* (Fig. 1). NMIIA, on the other hand, showed no clear correlation (Fig. 2 C).

To directly compare myosin II mechanoresponse and assembly state in individual cells, we next quantified the cortical enrichment of fluorescent myosin II. Fluorescence intensity line scans across individual cells were performed at the time when cells were initially contacted with the pipette (t = 0), avoiding the nucleus. NMIIA had low cortical enrichment with very little variation between the three cell types (Fig. 2 D). NMIIB had very little cortical enrichment in NIH 3T3 cells, moderate enrichment in Jurkat cells, and heavy enrichment in HeLa cells (Fig. 2 E). The level of enrichment was quantified for each cell by taking a ratio of background-corrected mean fluorescence intensity at the cell membrane to the intensity inside the cytoplasm (I_m/I_c; Fig. 2, F and G). While no significant difference was seen between the three cell types for NMIIA, NMIIB showed significant differences between each of the cell types (Fig. 2 G). This trend closely resembles the cytoskeletal association measured at a population level in Fig. 2 B. Plotting each cell as a function of peak mechanoresponse versus cortical enrichment (I_m/I_c) revealed that moderately enriched cells, with I_m/I_c values between 1.5 and 2.0, had the highest mechanoresponsiveness (Fig. 2 H). Each cell type clusters distinctly, with NIH 3T3 cells on the far left of the Gaussian fit, Jurkat cells in the center and high on the curve, and HeLa cells falling on the right (Fig. 2 H). When comparing the overall fluorescence intensity, the three cell types had no significant difference in myosin IIB expression (Fig. S1 A). However, mechanoresponsiveness does weakly negatively correlate with expression, especially in HeLa cells, but this trend does not alter the interpretation of the data (Fig. S1 B).

NMIIB heavy chain phosphomimetic and nonphosphorylatable mutants change cytoskeletal association and mechanoresponsiveness

To test whether altering the cortical enrichment of NMIIB is sufficient to change NMIIB mechanoresponsiveness in a single cell type, we expressed GFP-NMIIB constructs with phosphomimetic and nonphosphorylatable mutations in the tail domain. To do this, we focused on the 1935 residue, which is thought to be phosphorylated by PKCζ (Juanes-García et al., 2015). First, the fluorescence intensity of the constructs was similar between the mutants in both HeLa and NIH 3T3 cells (Fig. S2 A). For the 1935D and 1935A mutants, very little correlation was observed between fluorescence intensity and mechanoresponse in these two cell types (Fig. S2, B and C). The level of expression of the WT, 1935A, and 1935D fluorescent NMIIB constructs was quantified by Western analysis; no differences were detected between the three versions of fluorescent NMIIB (Fig. S2, D and E). This expression value was normalized to the transfection efficiency for each cell type to better estimate the level of overexpression in the cells being aspirated (Fig. S2 F). The ratio of fluorescent NMIIB to endogenous NMIIB was less than twofold for all three versions of fluorescent NMIIB in both cell types (Fig. S2 F).

In HeLa cells, the 1935D mutant had reduced initial enrichment in the cortex, compared with the 1935A mutant, and much higher mechanoresponsiveness than the 1935A mutant over 5 min (Fig. 3 A). Quantification of the Triton-insoluble cytoskeletal fraction of the 1935D in HeLa cells in suspension revealed a significantly lower value than WT endogenous NMIIB (Fig. 3 B and Fig. S2 G). In contrast, the 1935A mutant had significantly higher assembly than 1935D, but no difference as compared with WT (Fig. 3 D and Fig S2 G). Quantification of mechanoresponse kinetics was performed by normalizing the I_p/I_o value at each time point to the I_p/I_o at t = 0, then averaging each time point to create a single curve (Fig. 3 C; please note that for all kinetic traces, the zero-time point corresponds to the first frame in which the cell was captured by the pipette). While the 1935A mutant had a similar mechanoresponsiveness to WT NMIIB, the 1935D mutant had much higher mechanoresponsiveness (Fig. 3 C). Plotting the peak mechanoresponse as a function of initial cortical enrichment (fluorescent I_m/I_c ratio) for individual cells shows that all cells expressing NMIIB 1935A partition to the bottom right of the graph (shaded region) where most WT NMIIB cells are also found (Fig. 3 D). In contrast, the 1935D-expressing cells are found in the upper left portion of the graph (unshaded region; Fig. 3 D). Furthermore, the integrated fluorescence intensity, which serves as an indicator of total expression level, correlated poorly with the mechanoresponse for the three NMIIB mutants (Fig. S2 B). Overall, in HeLa cells, where a large fraction of NMIIB is associated with the cytoskeleton, reducing cytoskeletal association (1935D) improves mechanoresponsiveness.

To test whether increasing the cytoskeletal association of NMI IB would improve NMIIB mechanoresponsiveness in cells that have very low initial cytoskeletal association of NMIIB, we tested the same GFP-NMIIB phosphomimetic and nonphosphorylatable mutations in NIH 3T3s. Here, the 1935D mutant had very low initial cortical enrichment and no mechanoresponsiveness, while the 1935A mutant had increased cortical enrichment and mechanoresponsiveness over 5 min (Fig. 3, E and G). Specifically, the 1935D mutant in NIH 3T3 cells in suspension had a similar cytoskeletal association as WT endogenous NMIIB, while the 1935A mutant had a significant increase in the percent associated with the Triton-insoluble cytoskeleton (Fig. 3 F and Fig. S2 G). Plotting each cell as a function of initial cortical enrichment (I_m/I_c)

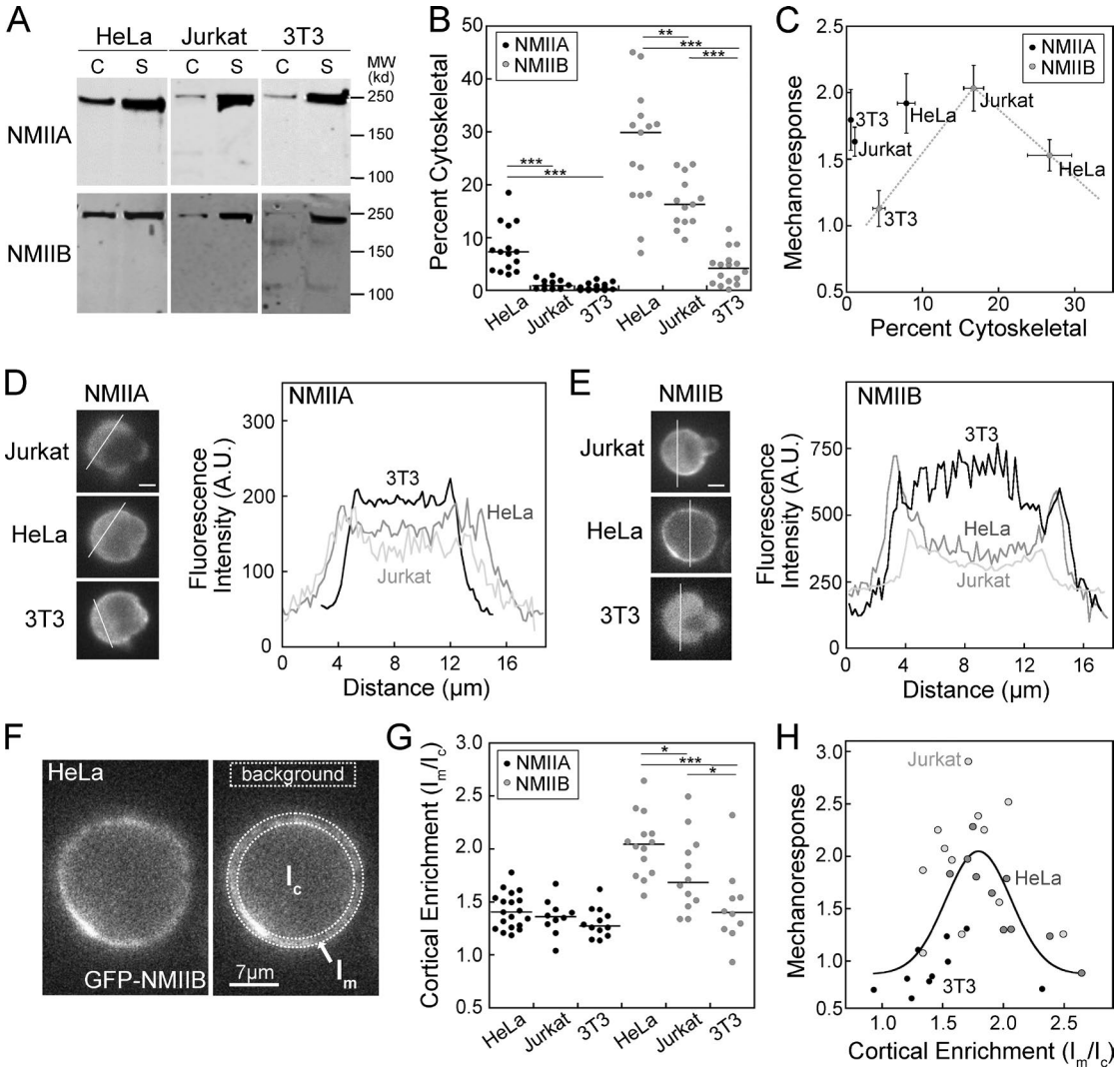

Figure 2. **Myosin IIB cytoskeletal association predicts mechanoresponsiveness in mammalian cells in a biphasic manner. (A and B)** Representative cytoskeletal assembly assay Western blots (A) show cytoskeletal (C) versus soluble (S) fractions, quantified in B, which shows median cytoskeletal association <10% for NMIIA and highly divergent median cytoskeletal association for NMIIB in HeLa, Jurkat, and NIH 3T3 cells. Each dot represents one fractionation tube, each experiment was performed over at least three separate days. **(C)** Plotting peak mechanoresponse (I_p/I_o) against percent cytoskeletal (from B) shows that NMIIB mechanoresponse is optimal in Jurkat cells, which have moderate cytoskeletal association among the three cell types. NMIIA shows no such relationship. Mechanoresponse values (y axis) were reproduced from Schiffhauer et al. (2016). **(D and E)** Representative intensity line scans of GFP-NMIIA (D) or GFP-NMIIB (E) at the initial frame of an MPA experiment demonstrate low initial cortical enrichment in three cell types for GFP-NMIIA, but divergent cortical enrichment for the three cell types for GFP-NMIIB. A.U., arbitrary units. **(F)** Representation of the quantification of cortical enrichment by comparing background-subtracted mean intensity in the membrane region (I_m) to that of the cytosolic region (I_c). **(G)** Quantification of cortical enrichment (I_m/I_c) in three cell types show no significant differences for GFP-NMIIA, but differences in GFP-NMIIB highly similar to the differences in B. Each dot represents one cell; each experiment was performed over at least two separate days. **(H)** Plotting each cell's peak mechanoresponse (I_p/I_o) as a function of its initial cortical enrichment value (I_m/I_c) shows a biphasic distribution similar to a Gaussian function. Mechanoresponse values (y axis) were reproduced from Schiffhauer et al. (2016). *, $P < 0.05$; **, $P < 0.005$; ***, $P < 0.0005$. Bars, 7 μm.

and peak mechanoresponse shows that all cells expressing NMIIB 1935D partition to the bottom left of the graph (Fig. 3 H; shaded region). In contrast, the 1935A-expressing cells are found in the upper right portion of the graph (Fig. 3 D; unshaded region). Comparison of fluorescence intensity with mechanoresponse for the three NMIIB mutants also revealed a very poor correlation between these parameters (Fig. S2 C). These data suggest that in NIH 3T3 cells, where a small fraction of NMIIB is associated with the cortex, increasing cytoskeletal association improves mechanoresponsiveness.

PKCζ expression and activity alters NMIIB cytoskeletal association and mechanoresponsiveness

To directly address the role of the kinase PKCζ in regulating the cytoskeletal association and mechanoresponsiveness of myosin II, we first measured the relative endogenous expression of the kinase in HeLa, Jurkat, and NIH 3T3 cells. NIH 3T3 cells showed the highest levels of PKCζ, followed by Jurkat then HeLa cells (Fig. 4 A). Comparing mean cortical enrichment (I_m/I_c) values for NMIIA and NMIIB (Fig. 2 G) to expression of PKCζ in the three cell types shows a steep negative correlation for NMIIB

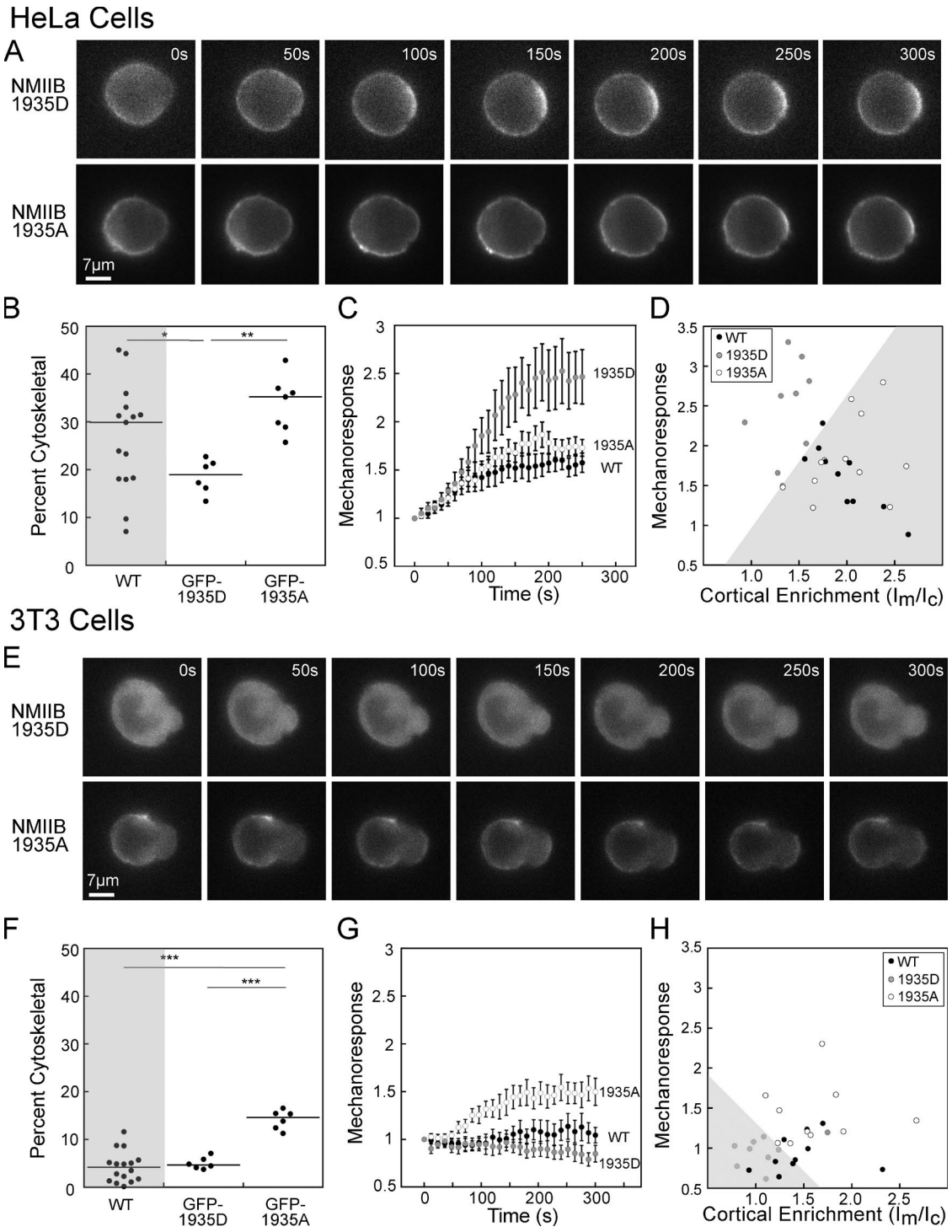

Figure 3. **Myosin IIB heavy chain phosphomimetic and nonphosphorylatable mutants change cytoskeletal association and mechanoresponsiveness.** **(A)** Representative time series for MPA of HeLa cells expressing GFP-tagged phosphomimetic (NMIIB 1935D) or nonphosphorylatable (NMIIB 1935A) mutants of NMIIB. **(B)** Quantification of cytoskeletal assembly of NMIIB in HeLa cells reveals a significant reduction in percent cytoskeletal for the 1935D mutant, but not for the 1935A mutant, compared with endogenous NMIIB (WT data reproduced from Fig. 2). **(C)** Accumulation during MPA over 250 s shows much more robust response for the 1935D mutant (n = 9) compared with the 1935A mutant (n = 12) or WT NMIIB (n = 10). **(D)** Plotting peak mechanoresponse and initial cortical enrichment (I_m/I_c) for each cell shows that all cells expressing the 1935A mutant are found in the lower right region of the graph (gray shaded region), while all cells expressing the 1935D mutant are found in the upper left region of the graph (unshaded region). **(E)** Representative time series for MPA of NIH 3T3 cells expressing GFP-tagged phosphomimetic (NMIIB 1935D) or nonphosphorylatable (NMIIB 1935A) mutants of NMIIB. **(F)** Quantification of cytoskeletal assembly of NMIIB in NIH 3T3 cells shows a highly significant enhancement in percent cytoskeletal for the 1935A mutant, but no significant change for the 1935D mutant compared with endogenous NMIIB (WT data reproduced from Fig. 2). **(G)** Accumulation during MPA over 250 s shows mechanoresponse for the 1935A mutant (n = 10), while no significant accumulation is seen for the 1935D mutant (n = 9) or WT NMIIB (n = 10). **(H)** Plotting peak mechanoresponse and initial cortical enrichment (I_m/I_c) for each cell shows that all cells expressing the 1935D mutant are found in the lower right region of the graph (gray shaded region), while all

(Fig. 4 A). The slope of the linear fit for NMIIB (−0.067) is more than fivefold steeper than the linear fit for NMIIA (−0.013). Due to the high expression of PKCζ and low cytoskeletal association of NMIIB in NIH 3T3 cells, we asked whether inhibition of PKCζ function, using a myristoylated PKCζ pseudosubstrate inhibitory peptide (Zeta-inhibitory peptide; ZIP), would affect the cytoskeletal association of NMIIB. The addition of 10 µM ZIP significantly increased the cytoskeletal association of NMIIB, but not NMIIA, in NIH 3T3 cells in suspension (Fig. 4 B). Treatment with the inhibitor also improved NMIIB mechanoresponsiveness, while NMIIA mechanoresponsiveness was unaffected (Fig. 4 C). The magnitude of NMIIB mechanoresponsiveness seen in the presence of ZIP is very similar to that of the NMIIB 1935A mutant in NIH 3T3 cells (Fig. 3 G). To test whether PKCζ's effect required phosphorylation at the 1935 residue, we tested mechanoresponse in cells expressing the 1935D mutant version of NMIIB. The inhibition of PKCζ was not sufficient to allow mechanoresponse in the NMIIB-1935D mutant (Fig. 4 C), suggesting that this residue is indeed critical for the effect of PKCζ on NMIIB. To rule out any other off-target effects of the ZIP, we used a second, specific small molecule inhibitor of atypical PKCs, 2-acetyl-1,3-cyclopentanedione (ACPD), at a concentration well below the IC50 of the compound for other PKC enzymes (2.5 µM; Sajan et al., 2014). ACPD treatment similarly improved NMIIB's mechanoresponsiveness in NIH 3T3 cells (Fig. S3 A).

In HeLa cells, where NMIIB cytoskeletal association is high (Fig. 2) and PKCζ expression is low, we tested the effect of overexpression and activation of PKCζ on NMIIB cytoskeletal association and mechanoresponsiveness. Overexpression was performed transiently with either WT PKCζ or myristoylated PKCζ, which is constitutively active due to anchorage on the plasma membrane. To confirm that the myristoylated PKCζ had the desired effect of increasing NMIIB phosphorylation as observed previously (Juanes-García et al., 2015), we performed quantitative mass spec using tandem mass tagging labeling and phospho-enrichment of lysates from HeLa cells and HeLa cells transfected with myristoylated PKCζ (Fig. S3 B). We found that phosphorylation indeed occurred at S1935 or S1937 (peptide analysis was unable to distinguish between these possibilities). Further, HeLa cells expressing myristoylated PKCζ had 1.9-fold higher phosphorylation at the S1935/1937 site than HeLa cells alone ($n = 3$; $P = 0.02$; Student's t test). Finally, we also assessed NIH 3T3 cells, which had a 2.8-fold higher phosphorylation at 1935/1937 than untransfected HeLa cells ($n = 2$). A phosphorylated residue was also detected at S1956 in all three conditions, but the level of this phosphorylation did not differ significantly between them.

Compared with overexpression of an empty plasmid, NMIIA cytoskeletal association was not altered upon PKCζ overexpression, myristoylated PKCζ overexpression, or treatment with PKCζ inhibitor (Fig. 4 D). However, NMIIB showed a significant reduction in the cytoskeletal fraction following 18-fold PKCζ and 10-fold myristoylated PKCζ overexpression (Fig. 4 E and Fig. S3, C and D). Inhibition of PKCζ using the ZIP did not significantly affect NMIIB cytoskeletal association (Fig. 4 E), which is consistent with the finding that the NMIIB 1935A mutant behaves like WT NMIIB in HeLa cells (Fig. 3, B and C). Interestingly, while the overexpression of WT PKCζ significantly increased NMIIB mechanoresponsiveness, the overexpression of myristoylated-PKCζ did not (Fig. 4 F). This effect is explained by the biphasic relationship between cytoskeletal association and mechanoresponsiveness, where pushing NMIIB cytoskeletal association too low results in suboptimal mechanoresponsiveness. While we did not detect a large difference in NMIIB percent cytoskeletal between WT and myristoylated overexpressers at a population level, on an individual cell level, myristoylated PKCζ–expressing cells showed significantly lower GFP-NMIIB cortical enrichment (Fig. S3 E). This discrepancy is explained by some masking of the phenotype at the population level by the portion of cells that remain untransfected. Furthermore, PKCζ itself did not undergo mechanoresponsive accumulation in HeLa cells, indicating that this enzyme establishes the assembly state of myosin II rather than directly responding to mechanical stress (Fig. S3 F).

We next sought to determine whether inputs controlling NMIIB assembly, other than PKCζ, could similarly perturb NMIIB mechanoresponsiveness. Due to the ability of NMIIA and NMIIB to coassemble into hetero-filaments (Beach et al., 2014; Shutova et al., 2014), we reasoned that NMIIA might affect the filament assembly properties of NMIIB in cells without perturbing other chemical signaling pathways. NMIIB assembly was indeed significantly higher in two HeLa NMIIA knockdown cell lines, compared with control (Fig. 5, A and C). The percent NMIIA knockdown achieved in shIIA-1 and shIIA-2 was 80 and 95%, respectively, while NMIIB showed no significant reduction in expression (Fig. 5 B). The large reduction in NMIIA expression in shIIA-2 is also accompanied by punctate distribution of GFP-NMIIB in the HeLa cortex (Fig. 5 D), implying that NMIIA influences the dynamics of NMIIB assembly and turnover. This increase in assembly results in a reduction of mechanoresponsiveness (Fig. 5 D), even with the NMIIB 1935D mutant. Overall, NMIIB's assembly state is the primary determinant of its mechanoresponsiveness, and it is through this parameter that PKCζ tunes NMIIB's mechanoaccumulation.

NMIIB mechanoresponsiveness depends on the fraction of free and assembled myosin II, not concentration of monomers

Since NMII accumulation is mediated by the addition of diffusing subunits to the mechanically loaded actomyosin network, we considered the possibility that the most sensitive parameter for mechanoresponsiveness was the concentration of free myosin in the cytosol. To measure total NMII concentration in cells, we compared endogenous NMIIA and NMIIB in HeLa cell lysates to known quantities of the purified tail fragment of NMIIA or

cells expressing the 1935A mutant are found in the upper right region of the graph (unshaded region). Mechanoresponse kinetic data for WT NMIIB in HeLa (C) and NIH 3T3 (G) cells reproduced from Schiffhauer et al. (2016). For percent cytoskeletal measurements, each dot represents one fractionation tube, and each condition was assessed over at least three separate days. For mechanoresponse, each dot represents one cell, each condition was assessed over at least two separate days. Error bars are SEM. *, $P < 0.05$; **, $P < 0.005$; ***, $P < 0.0005$.

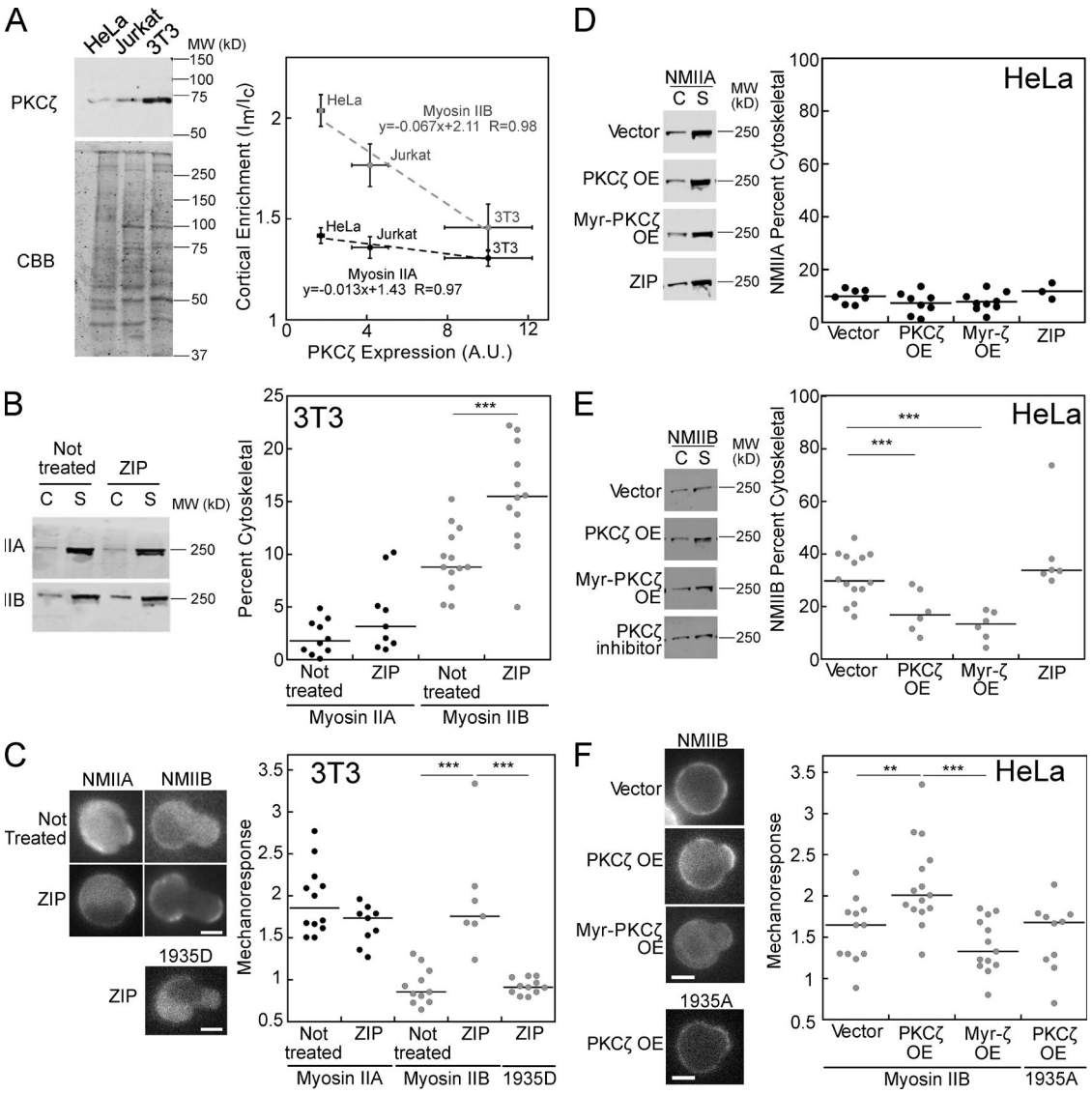

Figure 4. **PKCζ expression and activity alters NMIIB cytoskeletal association and mechanoresponse. (A)** PKCζ expression (n = 3) anti-correlates with NMII cortical enrichment, with fivefold steeper slope for NMIIB than NMIIA. A.U., arbitrary units. **(B)** PKCζ inhibition increases NMIIB cytoskeletal association and does not change NMIIA association in 3T3 cells, as measured by cytoskeletal (C) versus soluble (S) fractions. **(C)** Inhibition of PKCζ increases NMIIB mechanoresponse, but does not change NMIIA mechanoresponse and does not affect the NMIIB 1935D mutant in 3T3 cells. **(D)** Overexpression of PKCζ, constitutively active Myristoylated-PKCζ, or treatment with PKCζ inhibitor does not change NMIIA cytoskeletal association. **(E)** However, overexpression of PKCζ and Myr-PKCζ reduces the cytoskeletal association of NMIIB in HeLa cells, while PKCζ inhibitor has no effect. **(F)** PKCζ overexpression improves mechanoresponse in a manner dependent on the 1935S residue, while Myr-PKCζ overexpression shows no change in mechanoresponse in HeLa cells. For percent cytoskeletal measurements, each dot represents one fractionation tube, and each condition was assessed over at least three separate days. For mechanoresponse, each dot represents one cell and each condition was assessed over at least two separate days. Error bars are SEM; **, P < 0.005; ***, P < 0.0005. OE, overexpression. Bars, 7 µm.

NMIIB, which contains the antibody epitope (Fig. S4 A). We then compared the amount of NMIIA and NMIIB in Jurkat and NIH 3T3 cells, loaded with equal amounts of total protein (Fig. S4 B). This allowed for the calculation of the concentration of NMIIA and NMIIB in HeLa, Jurkat, and NIH 3T3 cells (Fig. S4 C). While relative amounts of NMIIA and NMIIB have been compared in several mammalian cell types (Pecci et al., 2018), to our knowledge, quantification of the concentration of NMIIA and NMIIB in mammalian cells has not been reported previously. The concentrations measured here, 200–550 nM NMIIA and 36–120 nM NMIIB, are similar to concentrations measured for the two myosin II isoforms in yeast (Myo2p: 450 nM and Myp2p: 380 nM; Wu and Pollard, 2005), but lower than the 3.4 µM found in *Dictyostelium* (Robinson et al., 2002). A comparison of NMIIB mechanoresponsiveness and the concentration of soluble NMIIB (calculated from total NMIIB and the percent soluble; Fig. 2 B) shows no obvious correlation (Fig. S4 D). However, the comparison of the percentage of NMIIB in the cytoskeletal fraction and NMIIB mechanoresponsiveness demonstrates a clear biphasic relationship (Fig. 6 A). All conditions tested here are included in this graph, along with two additional cell lines (HEK293 and Cos-7) which have been measured previously (Surcel et al., 2015;

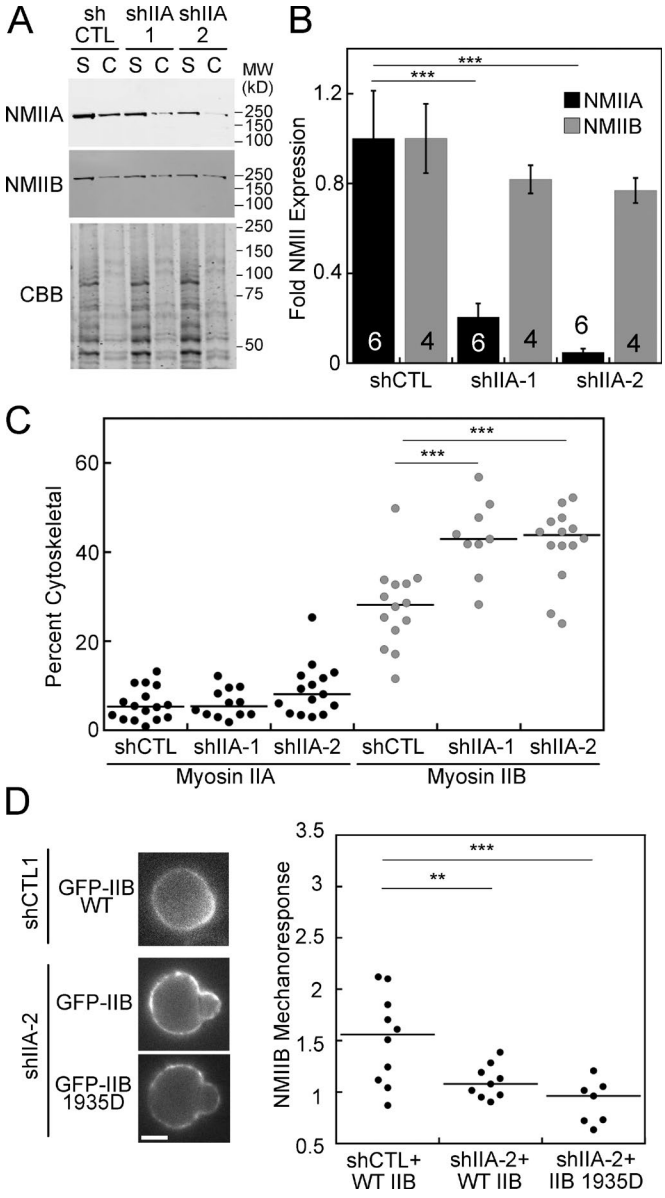

Figure 5. **NMIIA effects NMIIB cytoskeletal association and mechanoresponse. (A and B)** NMIIA expression is significantly reduced in two HeLa shRNA NMIIA knockdown lines, while NMIIB expression does not significantly change. **(A and C)** In the two shRNA NMIIA knockdown lines, NMIIB cytoskeletal association is increased, while the association of the remaining NMIIA does not change, as measured by cytoskeletal (C) and soluble (S) fractions. **(D)** GFP-NMIIB mechanoresponse is lost in the shIIA-2 knockdown line and is not rescued by the NMIIB 1935D mutant. *n* values displayed on bars; error bars are SEM. **, P < 0.005; ***, P < 0.0005. Bar, 7 µm.

Schiffhauer et al., 2016). Overall, the ability of NMIIB to respond to mechanical stress is dependent on the fraction of cytoskeletal-associated NMIIB with maximal mechanoresponsiveness occurring at an assembly fraction of ∼20%, very similar to what was observed in *Dictyostelium*.

Discussion

An open question in the field of mechanobiology concerns the molecular mechanisms by which chemical and mechanical signals are integrated by cells. While molecular systems where mechanical inputs are sensed and converted into chemical signals have been studied, systems where chemical inputs tune the ability of molecular machinery to sense and respond to forces are less well understood. We propose that in the case of NMIIB, chemical signals, including phosphorylation through myosin heavy chain kinases like PKCζ, indirectly control NMIIB mechanoresponsiveness. Our molecular model (Fig. 1 B) predicts that changing the rate at which myosin II monomers assemble into filaments will change the fraction of the myosin II in the cytoskeleton, and the assembly state of myosin II has to be optimal to produce mechanoresponsiveness. If myosin II has a low fraction of assembly and a low level of cytoskeletal association, the system does not have enough myosin II assembled in the cortex to sense and respond to the mechanical stress. We can also think of this condition in terms of rates of bipolar filament assembly. When the rates are exceedingly slow, myosin II is unable to dynamically build new structures at the site of applied stress. Conversely, when NMIIB has a high fraction of filament assembly and high level of cortical association, the cell cannot mount a mechanoresponse due to a poor differential between rates of assembly globally, as compared with the site of mechanical stress. Between these two conditions, when ∼20% of the myosin II is assembled in the cortex, and exchange rates between soluble myosin and cortical myosin are favorable, the system is poised to mount the maximal mechanoresponse (Fig. 6 B). In mammalian cells, as in *Dictyostelium*, the extent of myosin II filament assembly and cortical association are inversely related to the levels of heavy chain phosphorylation (Even-Faitelson and Ravid, 2006; Vicente-Manzanares et al., 2009; Dulyaninova and Bresnick, 2013; Juanes-García et al., 2015). Here, we find that the assembly state of NMIIB can be controlled by the heavy chain kinase PKCζ, resulting in a predictable change in the ability of NMIIB to accumulate in response to stress. Other perturbations that change the assembly state of NMIIB, such as the removal of NMIIA, also predictably change NMIIB's mechanoresponsiveness. Thus, the impact of heavy chain phosphorylation of NMIIB on its mechanoresponse is due to its impact on filament assembly and not a change in an unexplained molecular interaction.

Interestingly, the mechanism by which NMIIB localizes to the rear of migrating cells is dependent on both mechanical and chemical signaling cues. Raab et al. demonstrated that rear localization of NMIIB is mechanoresponsive; specifically, the occurrence of NMIIB polarization is dependent on substrate stiffness (Raab et al., 2012). On the other hand, Juanes-García et al. found that NMIIB localization is dependent on chemical signals driving phosphorylation of the heavy chain by PKCζ (Juanes-García et al., 2015). The integration of these signals that allow for proper NMIIB localization and function can be explained by the mechanism outlined in this study: PKCζ changes the NMIIB assembly state, which determines the ability of NMIIB to respond to mechanical stress. It is also worth considering that these sorts of biphasic relationships may be crucial to consider when designing treatment strategies for complex diseases, such as cancer. In some instances, it may be optimal to inhibit a process, but the same strategy may drive the system into a more aggressive, active state if the system is poised differently.

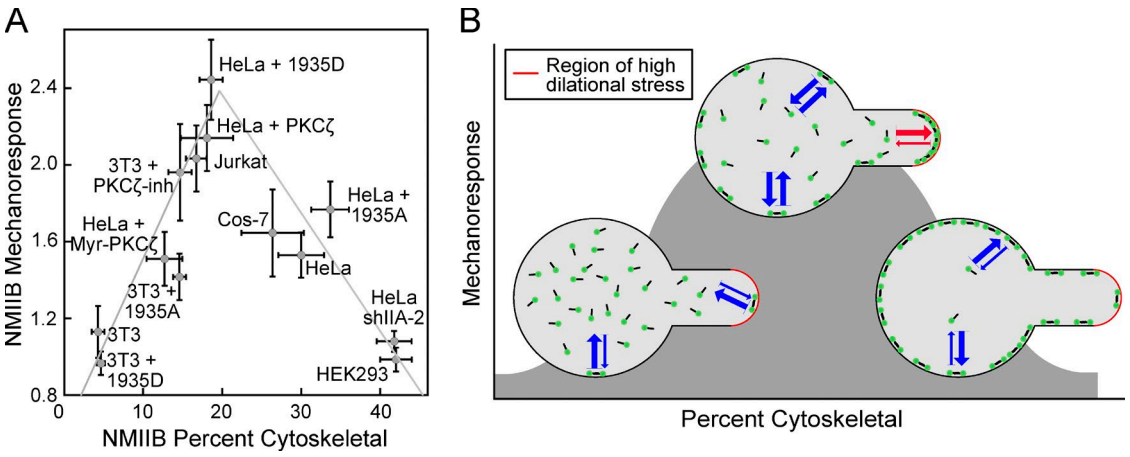

Figure 6. **Relationship between NMIIB mechanoresponsiveness and cytoskeletal association is biphasic. (A)** The fraction of NMIIB found in the cytoskeleton predicts NMIIB in a biphasic manner across many mammalian cell lines and conditions. **(B)** Graphical depiction of the relationship between cytoskeletal association and mechanoresponsiveness. If the NMIIB (green dots) balance is shifted to low fraction of assembly and a low level of cytoskeletal association, then the system is impaired in its ability to sense mechanical stress and then locally assemble new filaments, yielding a poor mechanoresponse. At the other extreme, if the NMIIB balance is shifted to have a high fraction of filament assembly and high level of cortical association, then similarly the NMIIB cannot mount a mechanoresponse. In between these extremes, when the appropriate free pool and level of cortical association of NMIIB is maintained, the system is poised to mount the maximal mechanoresponse. Error bars are SEM. Blue arrows represent on and off rates of NMIIB between the cytoplasm and the cortex. Red arrows represent these altered rates under localized mechanical stress.

Materials and methods

Model description

States considered

The computational model has been described previously (Luo et al., 2012, 2013; Mohan et al., 2015). In brief, we assumed that monomers exist in one of four states: assembly-incompetent, unbound (to actin) monomers ($\overline{M}$); assembly-competent, unbound monomers (M); assembly-incompetent, actin-bound monomers ($\overline{M}^*$); and assembly-competent, actin-bound monomers (M^*). The latter is the fundamental unit of bipolar filament assembly. Two of these monomers bind to form parallel dimers (D^*), which then subsequently associate in an anti-parallel fashion to form the tetramer (T^*). Subsequently, dimers add laterally to the bipolar tetramer to build the bipolar filaments, which range in size from 3 to 36 dimers for *Dictyostelium* myosin II. The assembly scheme describing this process is illustrated in Fig. 1 C, where the various interconversion parameters are given.

Interconversion between states

A full description of the interconversion between states has been described previously (Luo et al., 2012; Mohan et al., 2015). For the most part, interconversion between the various states was assumed to follow mass-action dynamics with constant rates. The exception is the rate constant k_{-1}, which describes myosin unbinding to actin and which is force dependent. In this case, we assumed a Bell-like molecular catch bond model and computed

$$k_{-1} = k_{-1}^0 \exp(-\Delta E_b/k_bT),$$

where k_{-1}^0 is the unbinding rate constant in the absence of force and cooperative interactions, and ΔE_b is the change in binding energy (E_b) associated with cooperative and force-dependent myosin II–actin binding. This is given by

$$\Delta E_b = \Delta E_s + \frac{Force}{\alpha myosin},$$

where myosin is the total concentration of the bound myosin. The first term, ΔE_s, is the change in strain energy associated with myosin–actin cooperative interactions and is given by the piecewise linear function:

$$\Delta E_s = \begin{cases} x_1\phi, \phi < \phi^* \\ x_1\phi^* + x_2(\phi - \phi^*), \phi \geq \phi^* \end{cases},$$

where $\phi = 3 \times myosin/C_{actin}$. The different nominal parameter values are given in Table 1 (Luo et al., 2012; Mohan et al., 2015).

Compartmental model

Spatially, we considered a compartmental model consisting of three compartments, one representing the cytoplasm and the other two representing two different cortical regions. One of these cortical regions represents the region of the cortex where aspiration pressure is applied, and the other represents the remaining cortex. The cell is assumed to be a sphere of radius R_c = 5 µm. The cortex forms a shell th = 350 nm thick on the outside of this sphere. We assume that the aspirating pipette has a radius of R_p = 2.5 µm and that the aspirated region forms a hemisphere of this radius. Thus, the total surface area of the cortex is $SA = 4\pi R_c^2$ of which $SA_p = 2\pi R_p^2$ experiences stress. Thus, the cytoplasm, cortex, aspirated cortex, and unaspirated cortex compartments have volumes defined as $V_{cytoplasm} = 4\pi(R_c - th)^3/3$, $V_{cortex} = 4\pi R_c^3/3 - V_{cytoplasm}$, $V_{asp\ cortex} = V_{cortex}(SA_p/SA)$, and $V_{unasp\ cortex} = V_{cortex}(1 - SA_p/SA)$.

Transfer between the different compartments is modeled by including a diffusive flux between the two cortical compartments and the cytoplasm. If D is the diffusion coefficient, then the flux per unit area is given by $-D\delta C/\delta x$, where C is the concentration of the species in question. For δx, we used the thickness of the cortex. The flux is in units of moles per unit area per time, and so we multiplied by the surface area of the interface computed above. To account for the effect on the concentration

Table 1. **Model parameters.**

Parameter	Value	Parameter	Value
k_+	0.05 $s^{-1}\mu M^{-1}$	k_-	0.59 s^{-1}
k_{on}	0.45 $s^{-1}\mu M^{-1}$		
k_1	$k_{on}C_{actin}$ s^{-1}	k_{-10}	300 s^{-1}
k_2	0.37 $s^{-1}\mu M^{-1}$	k_{-2}	0.01 s^{-1}
k_3	0.0396 $s^{-1}\mu M^{-1}$	k_{-3}	0.0045 s^{-1}
k_4	1.25 $s^{-1}\mu M^{-1}$	k_{-4}	0.025 s^{-1}
k_n, n > 4	2.50 $s^{-1}\mu M^{-1}$	k_{-n}, n > 4	0.2 s^{-1}
χ_1	11.11 k_BT nm	χ_2	1.92 k_BT nm
α	36	φ*	0.11
C_{actin}	Cytoplasm: 72 μM	myoII	3.4 μM
	Cortex: 79 μM		

of a molecule in a compartment, we need to divide by that compartment's volume.

We assumed that D = 0.8 $\mu m^2/s$ is the diffusion coefficient of unbound myosin monomers, as measured in *Drosophila* S2 cells (Uehara et al., 2010), which is very close to the diffusion coefficient for mCherry-myoII measured for this study in *Dictyostelium* by fluorescence correlation spectroscopy (FCS; 0.97 ± 0.35 $\mu m^2/s$). Bound monomers, dimers, and tetrameters diffuse at 1/400 this rate. Bipolar filaments having more than three dimers do not diffuse.

Simulation implementation

The model was simulated by solving differential equations for each of the states (40 states) in each of the three different compartments (120 total states). Initial conditions for each of the states were first computed in the absence of any external stress. Thereafter, for each set of parameters, differential equations were solved using MatLab's (Mathworks) ode23s stiff solver for 1000 s in the absence of force, followed by 300 s during which force F = 100k_bT was incorporated into the equation for k_{-1}.

Cell culture

Jurkat cells were cultured in RPMI 1640 (Sigma-Aldrich) with 10% FBS (Life Technologies). HeLa and NIH 3T3 cells were cultured in DMEM (Life Technologies) with 10% FBS. For MPA experiments, adherent cells were cultured on tissue-culture treated dishes (Corning), detached using 0.5% trypsin (Life Technologies), centrifuged, and resuspended in Leibovitz L-15 media (Life Technologies) with 10% FBS. Transient transfections were performed using FuGENE HD (Promega).

Constructs

GFP-tagged constructs for NMIIA (N-terminal label on gene *MYH9*; 11347; Addgene) and NMIIB (N-terminal label on gene *MYH10*; 11348; Addgene) were gifts from R. Adelstein (National Institutes of Health, Bethesda, MD). GFP-tagged NMIIB containing 1935D and 1935A mutations were gifts from M. Vincente-Manzanares (Instituto de Biologia Molecular y Cellular del Cancer, Salamanca, Spain; made by site-directed mutagenesis of the WT NMII constructs described above). pcDNA4-PKCZeta WT His-tagged was a gift from J. Wrana (University of Toronto, Toronto, Canada; C-terminal His tag on gene PRKCZ; 24609; Addgene). Myr.PKCzeta.FLAG was a gift from A. Toker (Harvard Medical School, Boston, MA; N-terminal myristoylation tag on gene PRKCZ; 10802; Addgene).

Engineered cell lines

NMIIA knockdown lines were generated in HeLa cells using constructs from the Broad Institute TRC shRNA library distributed as bacterial glycerol stocks by Open Biosystems. The negative control construct (TRC Lentiviral Nontargeting shRNA control; RHS6848) was 5′-CCGGTTGGTTTACATGTTGTGTGACTCGAG TCACACAACATGTAAACCATTTTTG-3′.

The following constructs were used to knockdown NMIIA: HeLa shIIA-1 (TRCN0000029467): 5′-CCGCGAAGTCAGCTCCCT AAA-3′; and HeLa shIIA-2 (TRCN0000029468): 5′-GCCAAGCTC AAGAACAAGCAT-3′.

Target plasmids were cotransfected with generation 2.0 lentiviral packaging plasmids psPAX.2 (12260; Addgene) and pMD2.G (12259; Addgene), gifts from D. Trono (École Polytechnique Fédérale de Lausanne, Lausanne, Switzerland), via TransIT 20/20 (Mirus) transfection reagent into Lenti-X HEK293t cells (Clontech). Lenti-X HEK293t cells were allowed to produce virus for 48 h, then media were collected and added to HeLa cultures. HeLa cells were treated with 5 μg/ml puromycin (Life Technologies) until growth of resistant cells occurred. Knockdown was verified by Western analysis.

Drug treatment

Myristoylated-PKCζ pseudosubstrate peptide inhibitor (Life Technologies) was dissolved in water and delivered to cells at 10 μM for 1 h before imaging or cell lysis. ACPD (Sigma-Aldrich) was dissolved in water and delivered to cells at 2.5 μM for 1 h before imaging.

Measurements of mechanosensory response using MPA

Mammalian cells expressing GFPs were trypsinized and loaded into the MPA observation chamber, which was filled with Leibovitz L-15 media at room temperature (Life Technologies). A pressure difference was generated by adjusting the height of a motor-driven water manometer. Cells were aspirated with a fixed pressure of 0.15 $nN/\mu m^2$ for NIH 3T3 cells and 0.2 $nN/\mu m^2$ for HeLa cells, due to the unique cortical tensions of these cells in an attempt to produce similar levels of cell deformation (Schiffhauer et al., 2016). All cells which demonstrated separation of cell membrane from the cortex at any time during recording were discarded. Images were collected every 10 s for 5 min with an Olympus IX81 microscope using a UPanFL 40× (1.30 NA) oil objective and an Andor iXON EMCCD camera. Acquisition was performed using Metamorph software and were analyzed using Image J (National Institutes of Health). After background correction, the fluorescence intensity (mean gray value) at the accumulation sites inside the micropipette were normalized against the opposite cortex of the cell (I_p/I_o). Measurements taken at the peak of mechanoresponse were then normalized against the initial I_p/I_o value to correct for any initial variation in cortical uniformity.

Western analysis

SDS-PAGE gels with 10% acrylamide were made in house, and transfers were performed at 90 V for 90 min. Blots were blocked in 5% dry milk in PBS + 0.1% Tween-20 (Sigma-Aldrich) and incubated with primary antibodies overnight in 5% milk in PBS-T. The NMIIA antibody used was Poly19098 (rabbit; 909801; BioLegend), the PKCζ antibody was H-1 (mouse; sc-17781; Santa Cruz), and the NMIIB antibody CMII 23 was from the Developmental Studies Hybridoma Bank (mouse; deposited by G. Conrad and A. Conrad, Kansas State University, Manhattan, KS). Blots were imaged using Li-Cor fluorescent secondary antibodies on the Li-Cor Odyssey CLx Blot Imager.

Cytoskeletal fractionation

Adherent mammalian cells were trypsinized (Jurkat cells are nonadherent) and rotated in media for 10 min to allow for stress fibers to collapse, leaving behind primarily cortical actin cytoskeleton that had been allowed to equilibrate following loss of cell adhesion. This condition reflects the cytoskeletal organization probed by MPA when measuring mechanoresponse. All three cell types were then lysed using a buffer containing 50 mM Pipes, pH 6.8, 46 mM NaCl, 2.5 mM EGTA, 1 mM ATP, 1 mM $MgCl_2$, and 0.5% Triton X-100, and a protease inhibitor cocktail containing Benzamidine, Leupeptin, Pepstatin A, TPCK, TLCK, Aprotinin, and PMSF (ionic strength was measured using conductance and found to be 17 mS/cm, equivalent to 150 mM NaCl).

Myosin quantification

Expression level of transiently expressed NMIIB was first compared with endogenous myosin by Western analysis. To correct for the fraction of cells expressing the fluorescently labeled NMIIB, the transfection efficiency in HeLa and 3T3 cells was calculated by measuring the number of fluorescent cells in a field using the Molecular Devices ImageXpress Micro XLS wide-field high-content analysis system. Cells were stained with Hoechst nuclear stain and imaged in the Hoechst (405 nm) and GFP (488 nm) channels. The images were then exported to MetaXpress high-content analysis software. A threshold level of GFP fluorescence was set using an untransfected sample, where a minimal number of cells were scored positively (<3%; Fig. S2 F). The total number of GFP-fluorescent cells was then measured in each transfection condition and compared with the total number of cells counted in the Hoechst channel.

To quantify endogenous NMIIA and NMIIB, cells were trypsinized, counted, and centrifuged into pellets containing 5×10^5 cells each. These pellets were washed in PBS, recentrifuged, and then lysed in 75 µl radioimmunoprecipitation assay lysis buffer plus 15 µl 6× SDS buffer. Due to cell volume and residual PBS, the total lysate volume reached 100 µl. 10 µl of lysate was added to each well of a 7% SDS-PAGE gel, or the equivalent of 5×10^4 cells/well. In addition, each well was spiked with a known quantity of purified myosin II tail fragment, containing the epitope region for the antibodies used, with sequential twofold dilutions. A 7% gel was used because it allowed for optimal transfer of both the large molecular weight endogenous myosin II and the smaller molecular weight purified tail fragment out of the gel. Transfer was most effective at a constant 45 V for 16 h, using polyvinylidene difluoride membranes to prevent smaller protein pass through and verifying complete transfer of larger proteins by performing a Coomassie stain to verify that no protein was left in the gel following transfer. The average volume of an individual cell for each cell type was determined from the MPA images, where cell radius is measured, and assuming the cell shape to be a sphere before aspiration. For each experiment, a standard curve was created from the spiked tail fragment to determine the total number of moles of endogenous myosin II in each lane. The number of cells per lane multiplied by the average volume of a single cell gave the total cell volume per lane, and concentration was determined from the ratio of these two values.

Statistical analysis

Statistical analysis was performed using KaleidaGraph (Synergy Software). Datasets were analyzed by ANOVA with a Fisher's least significant difference post hoc test. If datasets were not normally distributed, they were analyzed using a Kruskal-Wallis followed by a Mann-Whitney-Wilcoxon test.

Measurement of diffusion time by FCS

Dictyostelium cells transformed with mCherry-myoII were plated on glass dishes. FCS experiments were performed on interphase cells at ambient temperature (~20–23°C; normal growth temperatures for *Dictyostelium* cells) using a Zeiss AxioObserver with 780-Quasar confocal module and FCS, with a C-Apochromat 40× (NA 1.2) water objective. 100 nM Rhodamine 6G was used for pinhole alignment and structural parameter calculation. A structural parameter of six was used, and the confocal volume was measured to be 0.45 fL. Data were fit to a single-component 3D diffusion model, including a triplet-state component with an upper limit of 8 µs (Srivastava and Robinson, 2015; Kothari et al., 2017).

Quantitative mass spectrometry

The protein content from three biological replicates of the WT, knock-out, and treated knock-out cell lines were digested with trypsin, labeled with tandem mass tagging isobaric mass tags from Thermo Fisher, and combined (Thompson et al., 2003). One tenth of the pooled sample was step fractionated on reversed phase using 10 mM triethylammonium bicarbonate (pH ~9), eluting with 5, 10, 25, and 75% acetonitrile. The remainder of the pooled sample was enriched for phosphorylation on titanium oxide beads (Larsen et al., 2005). Each of the generated fractions was analyzed by multiplexed quantitative LC-tandem MS on an Orbitrap Lumos. To normalize the amount of MYH10 (NMIIB) across all samples, the relative abundance of MYH10 between samples was measured from reporter ion signal to noise values all MYH10, unique peptides detected in the reversed phase step fractions. This normalization was applied to the relative abundance of the phosphorylation peptides detected in the titanium oxide phospho-enriched fractions.

Online supplemental material

Fig. S1 shows magnitude of mechanoresponse is independent of intensity of GFP-NMIIB in different cell types. Fig. S2 shows

GFP-NMIIB 1935A and GFP-NMIIB 1935D expression in NIH 3T3 and HeLa cells does not correlate with mechanoresponse. Fig. S3 shows PKCζ activity controls mechanoresponse; however, PKCζ itself is not mechanoresponsive. Fig. S4 shows concentration of monomeric NMIIB in cells does not predict mechanoresponse.

Acknowledgments

We thank Simion Kreimer, PhD, and the Mass Spectrometry and Proteomics Facility at the Johns Hopkins School of Medicine for performing the quantitative mass spectrometry experiments. We thank the members of the Robinson laboratory for helpful discussions.

This work was supported by grants from National Institutes of Health (GM66817 and GM109863) and Defense Advanced Research Projects Agency (HR0011-16-C-0139). National Institutes of Health grant S10 OD016374 supported the purchase of the FCS instrument.

The authors declare no competing financial interests.

Author contributions: E.S. Schiffhauer provided conceptualization, project administration, data acquisition, data curation, formal analysis, visualization, writing of the original draft, review, and editing. V.A. Iglesias provided methodology and software. Y. Ren provided data acquisition. P. Kothari provided data acquisition, data curation, and draft editing. P.A. Iglesias provided methodology, software, conceptualization, and funding acquisition. D.N. Robinson provided conceptualization, funding acquisition, supervision, draft review, and editing.

Submitted: 8 June 2018
Revised: 20 November 2018
Accepted: 19 December 2018

References

Beach, J.R., L. Shao, K. Remmert, D. Li, E. Betzig, and J.A. Hammer III. 2014. Nonmuscle myosin II isoforms coassemble in living cells. *Curr. Biol.* 24:1160–1166. https://doi.org/10.1016/j.cub.2014.03.071

Billington, N., A. Wang, J. Mao, R.S. Adelstein, and J.R. Sellers. 2013. Characterization of three full-length human nonmuscle myosin II paralogs. *J. Biol. Chem.* 288:33398–33410. https://doi.org/10.1074/jbc.M113.499848

De la Roche, M.A., J.L. Smith, V. Betapudi, T.T. Egelhoff, and G.P. Côté. 2002. Signaling pathways regulating Dictyostelium myosin II. *J. Muscle Res. Cell Motil.* 23:703–718. https://doi.org/10.1023/A:1024467426244

Dulyaninova, N.G., and A.R. Bresnick. 2013. The heavy chain has its day: regulation of myosin-II assembly. *Bioarchitecture.* 3:77–85. https://doi.org/10.4161/bioa.26133

Dulyaninova, N.G., V.N. Malashkevich, S.C. Almo, and A.R. Bresnick. 2005. Regulation of myosin-IIA assembly and Mts1 binding by heavy chain phosphorylation. *Biochemistry.* 44:6867–6876. https://doi.org/10.1021/bi0500776

Etienne-Manneville, S., and A. Hall. 2001. Integrin-mediated activation of Cdc42 controls cell polarity in migrating astrocytes through PKCzeta. *Cell.* 106:489–498. https://doi.org/10.1016/S0092-8674(01)00471-8

Even-Faitelson, L., and S. Ravid. 2006. PAK1 and aPKCzeta regulate myosin II-B phosphorylation: a novel signaling pathway regulating filament assembly. *Mol. Biol. Cell.* 17:2869–2881. https://doi.org/10.1091/mbc.e05-11-1001

Fernandez-Gonzalez, R., S.M. Simoes, J.-C. Röper, S. Eaton, and J.A. Zallen. 2009. Myosin II dynamics are regulated by tension in intercalating cells. *Dev. Cell.* 17:736–743. https://doi.org/10.1016/j.devcel.2009.09.003

Finer, J.T., R.M. Simmons, and J.A. Spudich. 1994. Single myosin molecule mechanics: piconewton forces and nanometre steps. *Nature.* 368:113–119. https://doi.org/10.1038/368113a0

Gomes, E.R., S. Jani, and G.G. Gundersen. 2005. Nuclear movement regulated by Cdc42, MRCK, myosin, and actin flow establishes MTOC polarization in migrating cells. *Cell.* 121:451–463. https://doi.org/10.1016/j.cell.2005.02.022

Juanes-García, A., J.R. Chapman, R. Aguilar-Cuenca, C. Delgado-Arevalo, J. Hodges, L.A. Whitmore, J. Shabanowitz, D.F. Hunt, A.R. Horwitz, and M. Vicente-Manzanares. 2015. A regulatory motif in nonmuscle myosin II-B regulates its role in migratory front-back polarity. *J. Cell Biol.* 209:23–32. https://doi.org/10.1083/jcb.201407059

Kee, Y.-S., Y. Ren, D. Dorfman, M. Iijima, R. Firtel, P.A. Iglesias, and D.N. Robinson. 2012. A mechanosensory system governs myosin II accumulation in dividing cells. *Mol. Biol. Cell.* 23:1510–1523. https://doi.org/10.1091/mbc.e11-07-0601

Kim, J.H., Y. Ren, W.P. Ng, S. Li, S. Son, Y.-S. Kee, S. Zhang, G. Zhang, D.A. Fletcher, D.N. Robinson, and E.H. Chen. 2015. Mechanical tension drives cell membrane fusion. *Dev. Cell.* 32:561–573. https://doi.org/10.1016/j.devcel.2015.01.005

Kothari, P., E.S. Schiffhauer, and D.N. Robinson. 2017. Cytokinesis from nanometers to micrometers and microseconds to minutes. *Methods Cell Biol.* 137:307–322. https://doi.org/10.1016/bs.mcb.2016.03.038

Kovács, M., K. Thirumurugan, P.J. Knight, and J.R. Sellers. 2007. Load-dependent mechanism of nonmuscle myosin 2. *Proc. Natl. Acad. Sci. USA.* 104:9994–9999. https://doi.org/10.1073/pnas.0701181104

Larsen, M.R., T.E. Thingholm, O.N. Jensen, P. Roepstorff, and T.J.D. Jørgensen. 2005. Highly selective peptides from peptide mixtures using titanium dioxide microcolumns. *Mol. Cell. Proteomics.* 4:873–886. https://doi.org/10.1074/mcp.T500007-MCP200

Luo, T., K. Mohan, V. Srivastava, Y. Ren, P.A. Iglesias, and D.N. Robinson. 2012. Understanding the cooperative interaction between myosin II and actin cross-linkers mediated by actin filaments during mechanosensation. *Biophys. J.* 102:238–247. https://doi.org/10.1016/j.bpj.2011.12.020

Luo, T., K. Mohan, P.A. Iglesias, and D.N. Robinson. 2013. Molecular mechanisms of cellular mechanosensing. *Nat. Mater.* 12:1064–1071. https://doi.org/10.1038/nmat3772

Mahajan, R.K., and J.D. Pardee. 1996. Assembly mechanism of Dictyostelium myosin II: regulation by K+, Mg2+, and actin filaments. *Biochemistry.* 35:15504–15514. https://doi.org/10.1021/bi9618981

Mohan, K., T. Luo, D.N. Robinson, and P.A. Iglesias. 2015. Cell shape regulation through mechanosensory feedback control. *J. R. Soc. Interface.* 12:20150512. https://doi.org/10.1098/rsif.2015.0512

Orlova, A., and E.H. Egelman. 1997. Cooperative rigor binding of myosin to actin is a function of F-actin structure. *J. Mol. Biol.* 265:469–474. https://doi.org/10.1006/jmbi.1996.0761

Pecci, A., X. Ma, A. Savoia, and R.S. Adelstein. 2018. MYH9: Structure, functions and role of non-muscle myosin IIA in human disease. *Gene.* 664:152–167. https://doi.org/10.1016/j.gene.2018.04.048

Poirier, C.C., W.P. Ng, D.N. Robinson, and P.A. Iglesias. 2012. Deconvolution of the cellular force-generating subsystems that govern cytokinesis furrow ingression. *PLOS Comput. Biol.* 8:e1002467. https://doi.org/10.1371/journal.pcbi.1002467

Raab, M., J. Swift, P.C.D.P. Dingal, P. Shah, J.-W. Shin, and D.E. Discher. 2012. Crawling from soft to stiff matrix polarizes the cytoskeleton and phosphoregulates myosin-II heavy chain. *J. Cell Biol.* 199:669–683. https://doi.org/10.1083/jcb.201205056

Rai, V., and T.T. Egelhoff. 2011. Role of B regulatory subunits of protein phosphatase type 2A in myosin II assembly control in Dictyostelium discoideum. *Eukaryot. Cell.* 10:604–610. https://doi.org/10.1128/EC.00296-10

Ren, Y., J.C. Effler, M. Norstrom, T. Luo, R.A. Firtel, P.A. Iglesias, R.S. Rock, and D.N. Robinson. 2009. Mechanosensing through cooperative interactions between myosin II and the actin crosslinker cortexillin I. *Curr. Biol.* 19:1421–1428. https://doi.org/10.1016/j.cub.2009.07.018

Ren, Y., H. West-Foyle, A. Surcel, C. Miller, and D.N. Robinson. 2014. Genetic suppression of a phosphomimic myosin II identifies system-level factors that promote myosin II cleavage furrow accumulation. *Mol. Biol. Cell.* 25:4150–4165. https://doi.org/10.1091/mbc.e14-08-1322

Robinson, D.N., G. Cavet, H.M. Warrick, and J.A. Spudich. 2002. Quantitation of the distribution and flux of myosin-II during cytokinesis. *BMC Cell Biol.* 3:4. https://doi.org/10.1186/1471-2121-3-4

Sabry, J.H., S.L. Moores, S. Ryan, J.H. Zang, and J.A. Spudich. 1997. Myosin heavy chain phosphorylation sites regulate myosin localization during cytokinesis in live cells. *Mol. Biol. Cell.* 8:2605–2615. https://doi.org/10.1091/mbc.8.12.2605

Sajan, M.P., M.E. Acevedo-Duncan, M.L. Standaert, R.A. Ivey, M. Lee, and R.V. Farese. 2014. Akt-dependent phosphorylation of hepatic FoxO1 is compartmentalized on a WD40/ProF scaffold and is selectively inhibited by

aPKC in early phases of diet-induced obesity. *Diabetes.* 63:2690–2701. https://doi.org/10.2337/db13-1863

Schiffhauer, E.S., T. Luo, K. Mohan, V. Srivastava, X. Qian, E.R. Griffis, P.A. Iglesias, and D.N. Robinson. 2016. Mechanoaccumulative Elements of the Mammalian Actin Cytoskeleton. *Curr. Biol.* 26:1473–1479. https://doi.org/10.1016/j.cub.2016.04.007

Schiller, H.B., M.-R. Hermann, J. Polleux, T. Vignaud, S. Zanivan, C.C. Friedel, Z. Sun, A. Raducanu, K.-E. Gottschalk, M. Théry, et al. 2013. β1- and αv-class integrins cooperate to regulate myosin II during rigidity sensing of fibronectin-based microenvironments. *Nat. Cell Biol.* 15:625–636. https://doi.org/10.1038/ncb2747

Shutova, M.S., W.A. Spessott, C.G. Giraudo, and T. Svitkina. 2014. Endogenous species of mammalian nonmuscle myosin IIA and IIB include activated monomers and heteropolymers. *Curr. Biol.* 24:1958–1968. https://doi.org/10.1016/j.cub.2014.07.070

Srivastava, V., and D.N. Robinson. 2015. Mechanical stress and network structure drive protein dynamics during cytokinesis. *Curr. Biol.* 25:663–670. https://doi.org/10.1016/j.cub.2015.01.025

Surcel, A., W.P. Ng, H. West-Foyle, Q. Zhu, Y. Ren, L.B. Avery, A.K. Krenc, D.J. Meyers, R.S. Rock, R.A. Anders, et al. 2015. Pharmacological activation of myosin II paralogs to correct cell mechanics defects. *Proc. Natl. Acad. Sci. USA.* 112:1428–1433. https://doi.org/10.1073/pnas.1412592112

Thompson, A., J. Schäfer, K. Kuhn, S. Kienle, J. Schwarz, G. Schmidt, T. Neumann, R. Johnstone, A.K. Mohammed, and C. Hamon. 2003. Tandem mass tags: a novel quantification strategy for comparative analysis of complex protein mixtures by MS/MS. *Anal. Chem.* 75:1895–1904. https://doi.org/10.1021/ac0262560

Tokuraku, K., R. Kurogi, R. Toya, and T.Q.P. Uyeda. 2009. Novel mode of cooperative binding between myosin and Mg2+ -actin filaments in the presence of low concentrations of ATP. *J. Mol. Biol.* 386:149–162. https://doi.org/10.1016/j.jmb.2008.12.008

Uehara, R., G. Goshima, I. Mabuchi, R.D. Vale, J.A. Spudich, and E.R. Griffis. 2010. Determinants of myosin II cortical localization during cytokinesis. *Curr. Biol.* 20:1080–1085. https://doi.org/10.1016/j.cub.2010.04.058

Uyeda, T.Q.P., Y. Iwadate, N. Umeki, A. Nagasaki, and S. Yumura. 2011. Stretching actin filaments within cells enhances their affinity for the myosin II motor domain. *PLoS One.* 6:e26200. https://doi.org/10.1371/journal.pone.0026200

Vicente-Manzanares, M., X. Ma, R.S. Adelstein, and A.R. Horwitz. 2009. Cytoskeletal motors: Non-muscle myosin II takes centre stage in cell adhesion and migration. *Nat. Rev. Mol. Cell Biol.* 10:778–790. https://doi.org/10.1038/nrm2786

Wu, J.Q., and T.D. Pollard. 2005. Counting cytokinesis proteins globally and locally in fission yeast. *Science.* 310:310–314. https://doi.org/10.1126/science.1113230

Yumura, S., M. Yoshida, V. Betapudi, L.S. Licate, Y. Iwadate, A. Nagasaki, T.Q.P. Uyeda, and T.T. Egelhoff. 2005. Multiple myosin II heavy chain kinases: roles in filament assembly control and proper cytokinesis in Dictyostelium. *Mol. Biol. Cell.* 16:4256–4266. https://doi.org/10.1091/mbc.e05-03-0219